The Impact of Two Coupled Cirrus Microphysics–Radiation Parameterizations on the Temperature and Specific Humidity Biases in the Tropical Tropopause Layer in a Climate Model

ANTHONY J. BARAN, PETER HILL,[a] DAVID WALTERS, STEVEN C. HARDIMAN, AND KALLI FURTADO

Met Office, Exeter, United Kingdom

PAUL R. FIELD

Met Office, Exeter, and University of Leeds, Leeds, United Kingdom

JAMES MANNERS

Met Office, Exeter, United Kingdom

(Manuscript received 18 November 2015, in final form 7 April 2016)

ABSTRACT

The impact of two different coupled cirrus microphysics–radiation parameterizations on the zonally averaged temperature and humidity biases in the tropical tropopause layer (TTL) of a Met Office climate model configuration is assessed. One parameterization is based on a linear coupling between a model prognostic variable, the ice mass mixing ratio q_i, and the integral optical properties. The second is based on the integral optical properties being parameterized as functions of q_i and temperature, T_c, where the mass coefficients (i.e., scattering and extinction) are parameterized as nonlinear functions of the ratio between q_i and T_c. The cirrus microphysics parameterization is based on a moment estimation parameterization of the particle size distribution (PSD), which relates the mass moment (i.e., second moment if mass is proportional to size raised to the power of 2) of the PSD to all other PSD moments through the magnitude of the second moment and T_c. This same microphysics PSD parameterization is applied to calculate the integral optical properties used in both radiation parameterizations and, thus, ensures PSD and mass consistency between the cirrus microphysics and radiation schemes. In this paper, the temperature-non-dependent and temperature-dependent parameterizations are shown to increase and decrease the zonally averaged temperature biases in the TTL by about 1 K, respectively. The temperature-dependent radiation parameterization is further demonstrated to have a positive impact on the specific humidity biases in the TTL, as well as decreasing the shortwave and longwave biases in the cloudy radiative effect. The temperature-dependent radiation parameterization is shown to be more consistent with TTL and global radiation observations.

1. Introduction

It is well known that cirrus makes an important contribution to the radiative balance of the tropical tropopause layer (TTL) through its temperature, spatial distributions, opacity, and composition. Moreover, it influences the water vapor concentration in the stratosphere (Heymsfield 1986; Sassen et al. 1989; McFarquhar et al. 2000; Corti et al. 2006; Wang and Dessler 2006; Stubenrauch et al. 2007; Jensen et al. 2008; Mace et al. 2009; Yang et al. 2010; Schwartz and Mace 2010; Taylor et al. 2011; Zhou et al. 2014; Hong and Liu 2015; Hardiman et al. 2015, and references therein).

[a] Current affiliation: Department of Meteorology, University of Reading, Reading, United Kingdom.

Corresponding author address: Dr. Anthony J. Baran, Met Office, Cordouan 2, FitzRoy Road, Exeter, Devon EX1 3PB, United Kingdom.
E-mail: anthony.baran@metoffice.gov.uk

DOI: 10.1175/JCLI-D-15-0821.1

Publisher's Note: This article was revised on 9 August 2016 to correct the spelling of the fourth author's name.

Typical TTL cirrus will efficiently trap outgoing longwave radiation from the surface and atmosphere, generally leading to a warming of the surface, and absorb incoming shortwave radiation at near-infrared wavelengths, generally leading to a local heating of the upper troposphere (Liou 1986; Liou 2005; Edwards et al. 2007; Baran 2009; Taylor et al. 2011; Baran 2012; Yi et al. 2013; Zhou et al. 2014; Hong and Liu 2015; Yang et al. 2015; Hardiman et al. 2015). The balance between cirrus warming or cooling the upper troposphere depends on its visible optical depth, as shown by Hong and Liu (2015), who demonstrated that cirrus with visible optical depths less than unity leads to a net heating of the upper troposphere, while optically thicker cirrus results in a net cooling of the upper troposphere. Moreover, subvisual cirrus occurs in the TTL, as found by Lawson et al. (2008); also, Lee et al. (2009) showed that these clouds may exert a net radiative effect on the order of about 1.1 $\mathrm{W\,m^{-2}}$.

In general, the role of cirrus in either heating or cooling the TTL depends not only on the visible optical depth but also on the microphysics and the scattering and absorption properties of atmospheric ice (Baran et al. 2014a, hereinafter B014a; Yang et al. 2015, and references therein). There have been aircraft campaigns that have examined the ice microphysics composition of the TTL. In the study by Heymsfield (1986), the common occurrence of trigonal particles was reported but more recent studies by Lawson et al. (2008) have found few occurrences of trigonal ice particles. In the study by McFarquhar et al. (2000), they found habit mixtures comprising 50% of hexagonal columns and trigonal ice crystals in the subvisual TTL cirrus they studied. Meanwhile, Lawson et al. (2008) found the occurrence of quasi-spherical ice particles to be the most common particle type for all crystal sizes. However, it is uncertain as to whether these particles are actually quasi-spherical due to the limiting resolving power of the microphysics instrumentation used at the time; therefore, the appearance of quasi-sphericity could be due to diffractive and optical effects, as noted by Cotton et al. (2010) and references therein. On the other hand, these particles could be quasi-spherical, but instruments are required that can adequately resolve these ice crystals of an uncertain shape, such as the small ice detector described in Ulanowski et al. (2006). For crystal sizes greater than 65 μm, Lawson et al. (2008) found habit mixtures comprising mostly hexagonal plates and irregular ice crystals. In the study by Jensen et al. (2008) they noted the occurrence of hexagonal plate aspect ratios of 6:1 of nearly 100 μm in size near the TTL, which were reported to be unassociated with deep tropical convection. The more recent Airborne Tropical Tropopause Experiment (ATTREX) reported by Jensen et al. (2016) found bullet rosettes to be commonly occurring with little evidence of aggregated ice crystals in the cirrus cases they sampled. The two particle size distributions shown in Jensen et al. (2016) extend to maximum dimensions of about 50 μm and almost 200 μm, at temperatures of $<$195 K and between about 195 and less than 210 K, respectively. Meanwhile, Lawson et al. (2008) report particle distributions extending to 165 μm in the subvisual TTL cirrus they sampled, which contrasts with the study of McFarquhar et al. (2000), who found that particle maximum dimensions did not extend to beyond 50 μm. Determining the habit mixtures and particle distributions in TTL cirrus is important, as the choice of assumed particle distributions in climate models will influence their predicted radiative effect of cirrus. For instance, in the study of Mitchell et al. (2008) they show that by assuming two different parameterizations of the small ice mode, the shortwave radiative effect differences in the annual zonally averaged fluxes at the top of the atmosphere in the tropics can be up to about $-25\,\mathrm{W\,m^{-2}}$. They also show that the longwave differences in the tropics can be up to $20\,\mathrm{W\,m^{-2}}$. Clearly, from the studies cited above, there is uncertainty as to the most general ice microphysics composition in the TTL to assume in models; in turn, this will affect climate model simulations of the TTL, as differing climate models assume dissimilar microphysics properties, which may lead to an excess in TTL warming or cooling (Hardiman et al. 2015). Further campaigns in the TTL are necessary if such uncertainties reported by Hardiman et al. (2015) are to be reduced in climate models. However, recent TTL process studies by Hardiman et al. (2015) have shown that physically improved climate model parameterizations do not necessarily improve simulations of the TTL. For example, recent parameterizations of cirrus microphysics and bulk optical properties by Furtado et al. (2015) and B014a, respectively, were shown to increase the temperature and specific humidity biases in the TTL in recent global configurations of the Met Office Unified Model (MetUM). In this paper, the physical reasons are explored as to why the parameterizations of Baran et al. (2014b, hereinafter B014b) increased the TTL temperature bias in the climate model. This paper also presents a new bulk optical property parameterization of cirrus that is demonstrated to provide a more accurate simulation of the TTL in the MetUM as well as an improved representation of MetUM simulations of the cloudy shortwave and longwave radiative effects. The paper is organized as follows: Section 2 describes the bulk optical property parameterization and its accuracy, and includes comparisons between the new and the B014b parameterizations. Section 3 briefly describes a baseline

MetUM configuration and compares the impact of the new and B014b parameterizations on this configuration against both observations and analyses. Section 4 discusses the results.

2. The parameterization

The parameterization presented in this paper is based on the ensemble model of cirrus ice crystals fully described in Baran and Labonnote (2007), whereby the bulk optical properties are derived by averaging habit-dependent, single-scattering properties over an assumed particle size distribution (PSD); a figure of the model is shown in Fig. 2 in B014b. A brief description of the model is given here. The ensemble model consists of six shapes, and these are a hexagonal ice column of an assumed aspect ratio (AR) of unity, the six-branched bullet rosette, and then hexagonal monomers are randomly attached to build four ice aggregate models, which consist of 3-, 5-, 8-, and, finally, 10-branched hexagonal ice aggregates. The latter aggregate models can cover the largest ice crystal sizes found in the PSD, while the former members can populate the smaller end of the ice crystal PSD. Alternatively, weights can be assigned to each member of the ensemble model at each PSD bin size to compute the bulk optical properties. Here, use is also made of the same bulk ice optical property database that was used to develop the B014b parameterization. The database is composed of the following bulk optical properties: the extinction and scattering coefficients, the single-scattering albedo ω_0, and the asymmetry parameter g. These bulk optical properties are defined by Eqs. (1)–(3) in B014b, and the same definitions are used in this paper. A full description of that database can be found in B014a and B014b. However, brief descriptions of the bulk optical property database and its experimental validation are given here. The database described in B014a consists of 20 662 values of ice water content (IWC) and T_c, which were compiled from a number of cirrus field campaigns described in Baran et al. (2011a), and these in situ campaigns were predominantly located between northern Europe and the tropics. However, most of the in situ IWC values that were compiled by Baran et al. (2011a) were not obtained at temperatures colder than −60°C. Because of this lack of in situ ice microphysics measurements down to temperatures as low as −80°C, in B014a, IWC values were randomly selected from temperatures warmer than −60°C and placed at temperatures between −60° and −80°C. In this way, the IWC and T_c space was built up to 20 662 values, which ranged between about 3.0×10^{-3} and about $10^{-9}\,\mathrm{kg\,m^{-3}}$, and between about −80° and 0°C, respectively. This range in IWC and T_c is sufficient to cover the range in IWC and T_c values that are likely to be predicted in the MetUM.

In B014a and B014b, the IWC and T_c values were related to the PSD through a moment estimation parameterization of the PSD ascribed to Field et al. (2007, hereafter F07) and this parameterization is further described below. The IWC–T_c generated PSDs were previously applied to the ensemble model single-scattering properties described in B014a to obtain the cirrus bulk optical properties used in B014b at 145 wavelengths between 0.20 and 120 μm. The same bulk ice optical properties utilized in B014b are used in this paper.

The coupled IWC–T_c bulk ice optical properties used in this paper have been validated using a variety of aircraft- and space-based solar and infrared radiometric measurements. For instance, in B014a the ensemble model bulk ice optical properties were applied to a fast radiative transfer model to simulate very high-resolution solar (between about 3.4 and 4.1 μm) and infrared (between about 8.0 and 12.0 μm) aircraft-based brightness temperature measurements obtained from directly above midlatitude cirrus of visible optical depth varying between about 0.03 and 0.06. It is shown in the paper that the solar and infrared brightness temperature measurements were mostly simulated to within ±2 and ±1 K, respectively. Note also that the lower visible optical depth of 0.03 is generally taken as the upper limit for ''subvisual'' cirrus, as defined by Sassen and Cho (1992). Moreover, B014a also showed that the same ensemble microphysical model could forward model deep frontal cirrus effective radar reflectivity at 35 GHz and microwave brightness temperatures at 190 GHz to generally within ±2 dBZ_e and ±2 K, respectively. Thus, B014a showed that, in the case of the solar and infrared measurements, the same microphysical model can be consistently applied across the spectrum using a full set of optical properties (i.e., the scattering phase function and integral optical properties) to simulate those observations. Meanwhile, Sourdeval et al. (2015) demonstrated that the same ensemble model bulk ice optical properties used in B014a could also replicate Cloud–Aerosol Lidar with Orthogonal Polarization (CALIOP) and in situ polar nephelometer measurements of the volume extinction coefficient of midlatitude cirrus to generally within the standard deviation of both CALIOP and polar nephelometer measurements. The in situ and CALIOP volume extinction coefficients varied between less than about 0.2 and 1.4 $\mathrm{km^{-1}}$, at the wavelengths of 0.532 and 0.80 μm, respectively. The ensemble

model's predicted bulk optical properties have also been globally validated by Vidot et al. (2015) and Letu et al. (2015).

In Vidot et al. (2015) it is shown that an equivalent weighting of 0.30, 0.30, 0.10, 0.20, and 0.10 applied to each of the ensemble habit extinction and scattering coefficients at each bin size of the F07 PSD parameterization best simulated cirrus infrared brightness temperature measurements from the Imaging Infrared Radiometer (IIR) instrument at wavelengths of 8.65, 10.60, and 12.05 μm. The combined mean brightness temperature bias using the weighted model optical properties was found to be only 0.43 K with a standard deviation of 6.85 K for visible optical depths between 0.03 and 4.0. The IIR brightness temperature simulations were based on more than 26000 profiles of IWC from the Cloudsat and CALIPSO Ice Cloud Property Product (2C-ICE) and radar–lidar (DARDAR) products (Deng et al. 2010; Delanoë and Hogan 2010). The IWC product profiles and atmospheric profiles (the latter profiles came from the European Centre for Medium-Range Weather Forecasts and were collocated with CALIOP) were located between the latitudes of about ±60° and at altitudes between about 440 and 50 hPa, thus covering the region of the TTL, and most of the profiles were located in the tropics. Meanwhile, Letu et al. (2015) used global observations from the Polarization and Directionality of the Earth's Reflectances-3 (POLDER-3) measurements on board the Polarization and Anisotropy of Reflectances for Atmospheric Sciences coupled with Observations from a Lidar (PARASOL) to show that the ensemble model's predicted ice cloud solar optical depths at a wavelength of 0.865 μm best minimized differences between observations, with all ice crystal models considered. The POLDER-3 analysis of Letu et al. (2015) is based on 589246 pixels, with each pixel size being approximately 6 km × 6 km. In most pixels the scattering angle range covered is between 60° and 160°, and in some pixels the scattering angle range covered is between 160° and 180°. The pixels were located between the latitudes of about ±90°, but the vast majority of pixels were located at latitudes between about ±60°. The data cover the period between the 20th and 22nd of March, June, September, and December 2008. Therefore, all meteorological seasons are covered in the time period studied by Letu et al. (2015) and the study is, thus far, the most comprehensive and consistent analysis of POLDER-3 global data. Given the preceding evidence, the ensemble model bulk ice optical properties have been sufficiently validated globally to apply to a parameterization of cirrus optical properties in a climate model. Such validation exercises described above are necessary to carry out to show that the full set of optical properties is consistent with measurements from across the spectrum in order to provide confidence in their applicability to climate models. As a further example of this validation approach, see, for example, the paper by Holz et al. (2016).

The PSDs applied to the ensemble model single-scattering properties in the preceding literature assumed the F07 moment estimation parameterization of the PSD. A full derivation of the PSD parameterization is given in F07, but a brief description is given here. The F07 parameterization is based on 10000 in situ measurements of the PSD and IWC, which were measured between the temperatures of 0° and −60°C during a number of cirrus field campaigns located in the midlatitudes and tropics. The parameterization is based on the moments of the PSD, given by the integral product of D^n and $f(D)$, where D is the maximum dimension of the ice crystal and $f(D)$ is the PSD, which gives the particle number concentration at each D, and $n \geq 0$. Therefore, the zeroth moment (i.e., $n = 0$) is the total number concentration of particles per unit volume of cloudy air. The PSD parameterization is related to the total IWC through some assumed relationship between mass and D, where in the case of aggregating ice crystals the mass of ice $\propto D^2$ (Westbrook et al. 2004; Cotton et al. 2013, and references therein). The other moments of the PSD are related to the second moment (M_2) through a relationship of the form $M_n = \sigma_n {M_2}^{\beta_n}$, where σ_n and β_n are functions of T_c. Therefore, given all M_n, the full PSD can be estimated from the IWC and T_c values via an assumed mass–dimensional relationship. It should be noted here that to reduce the impact of ice crystal shattering on the PSD parameterization, the in situ PSDs in F07 were filtered by using the measured interarrival times of the ice crystals as described in F07 and Field et al. (2006), and ice crystals with $D <$ 100 μm were ignored. However, the PSD parameterization does not ignore the shape of the ice crystal PSD at $D <$ 100 μm, but instead assumes an exponential PSD (Field and Heymsfield 2003) that is added to a modified gamma distribution at an ice crystal size of about 100 μm. The degree to which in situ PSDs are skewed due to ice crystal shattering has more recently been studied by Korolev et al. (2013). In that paper, they found that if filtering alone is applied without any modifications to the in situ microphysics probes on board aircraft, such as the use of antishatter tips, the PSD becomes significantly skewed from the best measured PSD at $D \leq$ 200–175 μm, where the best-measured PSDs were determined using both antishatter tips and filtering. Korolev et al. (2013) state that the precise ice crystal size at which significant divergence

from the best-estimated PSD occurs cannot as yet be determined due to insufficient statistical sampling of ice clouds. In other words, there are too few cirrus field campaigns on which to base firm conclusions. Therefore, it is currently unknown to what degree the F07 parameterization has been affected by the shattering of ice. However, this parameterization is more representative of cirrus PSDs than the Houze et al. (1979) PSD parameterization, which is the current assumption in the MetUM operational model. The Houze et al. (1979) parameterization is based on 37 in situ PSDs, 90% of which were measured at temperatures warmer than −30°C. Currently, within the operational MetUM, the Houze et al. (1979) estimated PSD is kept constant at temperatures colder than −35°C. This assumption means that at much colder temperatures, such as those that occur within the TTL region, there will be orders of magnitude more frequently occurring large ice crystals than there should be. This has clear implications for the assumed fall speed of ice crystals within the MetUM model, which must be artificially increased to several meters per second to accommodate space-based radiometric shortwave and outgoing longwave measurements of flux at the top of the atmosphere (TOA).

The F07 parameterization has been experimentally validated by Baran et al. (2011b) and Furtado et al. (2015). In Baran et al. (2011b) the moment estimated PSD was found to fit well to several cases of averaged in situ measured tropical PSDs. For several cases of midlatitude cirrus Furtado et al. (2015) compared the F07 moments to in situ measured moments, while ignoring particles less than 100 μm in size because of the current uncertainties in measuring the size of small ice at $D < 100\,\mu$m, and found good correlations between the parameterization and measurements for all cases considered. However, poor correlations emerged in that study when the moments predicted by the Houze et al. (1979) parameterization were compared against the in situ derived moments. The study of Furtado et al. (2015) emphasizes that the F07 parameterization is a better representation of the ice PSD to apply to climate models in general than the Houze et al. (1979) parameterization. This last statement is especially true in the TTL, given the above description of the Houze et al. (1979) parameterization.

Given that the F07 PSDs are related to a model prognostic variable (i.e., the mass carrying moment M_2) and this varies as a function of T_c, given that the ensemble model single-scattering properties have been integrated over these PSDs, the bulk ice optical properties can also be directly related to the climate model prognostic variable IWC [i.e., $m(D) = \text{constant} \times D^2$, where m is the mass (in kg)] and T_c or just IWC (as is the case in B014b). The behavior of the 20 662 bulk ice optical properties, ω_0 and g, in M_2–T_c space, is shown in Figs. 1a and 1b, respectively, at a wavelength of 1.575 μm. This wavelength is chosen as an example to show the variation of the bulk ice optical properties in the full space used for the later parameterizations. In Fig. 1a, it is shown that ω_0 varies between the values of 0.7 and 1.0, at the coldest temperature values, down to about −80°C and $M_2 \sim 10^{-5}\,\text{m}^{-1}$, and ω_0 is near unity. At these values of M_2 and T_c, the PSD is very narrow and will be largely composed of small ice crystals with many fewer occurring large ice crystals; therefore at this wavelength the smaller ice crystals will efficiently scatter incident radiation. At much larger values of M_2 and at much warmer temperatures, at $0.01\,\text{m}^{-1}$ and −15°C, respectively, the value of ω_0 decreases to a value of about 0.8. At such M_2 and T_c values, the PSD becomes much broader than previously, with much more frequently occurring large ice crystals, which at this wavelength will absorb incident radiation, thereby decreasing ω_0. The converse behavior is shown, at the same values of M_2 and T_c, for g in Fig. 1b, where g has the corresponding values of about 0.78 and 0.88. The reasons for these values are the same as those given for the behavior of ω_0. Figures 1a and 1b show that the spatial distribution of ω_0 and g is physically to expectation and would be a similar distribution if the optical properties were plotted as a function of some characteristic size. Here, we demonstrate this using the characteristic size usually assumed in radiation schemes in climate models, which is the mean effective dimension, D_{eff}, defined after Foot (1988) as

$$D_{\text{eff}} = \frac{\text{mass}_t}{\rho A_t}, \tag{1}$$

where in Eq. (1) mass_t and A_t are the total mass and orientation-averaged projected area of the PSD, respectively, and ρ is the density of solid ice. Here, we assume that $\rho = 1000\,\text{kg}\,\text{m}^{-3}$ to keep units in Eq. (1) consistent, hence the units of mass_t and A_t being in SI. First, we show that the moment M_2 can easily be related to D_{eff}, as shown in Fig. 2, where in Fig. 2, as an example, we assume that the mass_t and A_t are computed from the first member of the ensemble model, which is the hexagonal ice column of AR = 1.0. As can be seen from Fig. 2, the second moment or, equivalently, IWC (by assuming some mass–D relationship) could easily be related to D_{eff} as a function of T_c or just by relating IWC directly to D_{eff} by using some fitting procedure. Indeed, this latter approach was used by McFarquhar et al. (2003), who parameterized IWC explicitly as a function of an effective radius [D_{eff} can be related to the effective radius, r_{eff}, by $r_{\text{eff}} = (3/4) \times D_{\text{eff}}$]. Therefore, the bulk ice

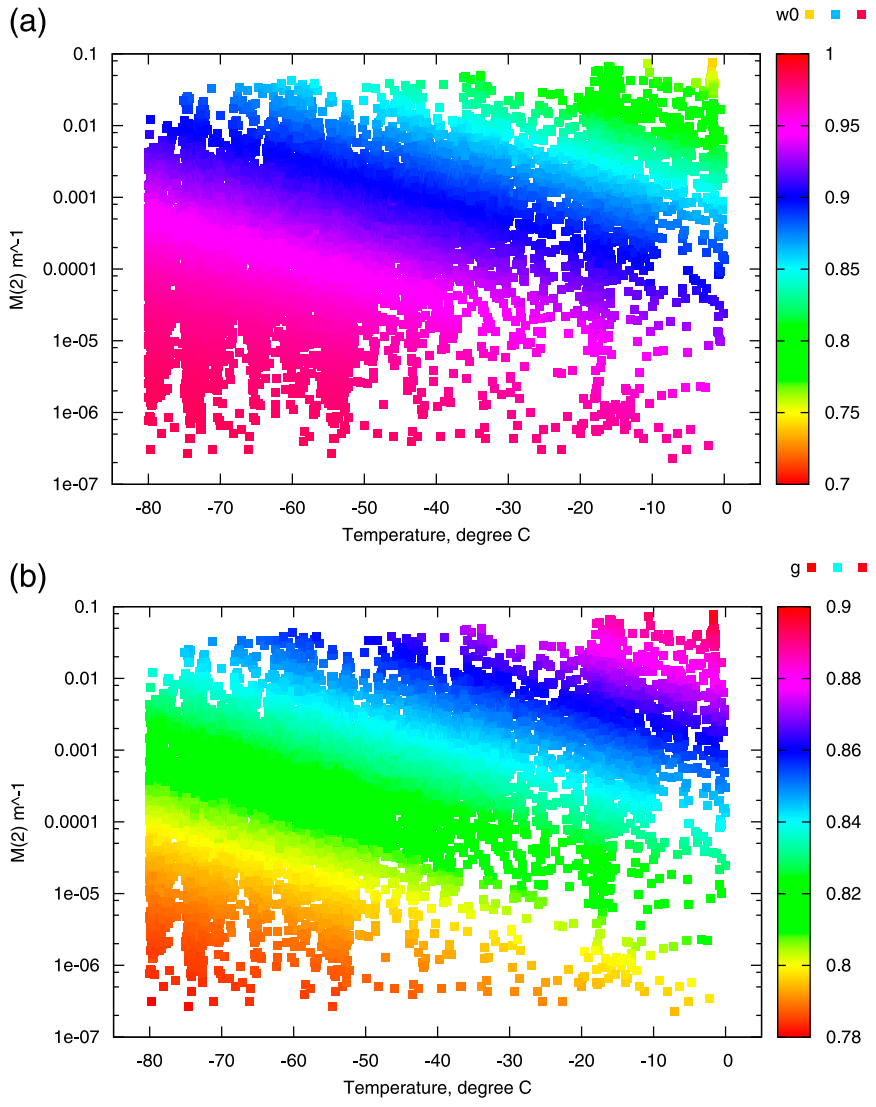

FIG. 1. The bulk optical properties (a) ω_0 and (b) g as a function of the mass carrying moment M(2) and temperature at the wavelength of 1.575 μm for all 20 662 values. The calculated values for ω_0 and g are shown as the color bar on the right-hand side of the figures.

optical properties can also be easily parameterized as a function of M_2 or IWC and T_c, as is done in B014b (i.e., IWC alone) and in this paper (i.e., IWC and T_c). We note that, for aggregating ice crystals both mass and diameter are proportional to D^2, so D_{eff} becomes independent of IWC. A further characteristic size could also be defined, such as the ratio between the third and second moments of the PSD. If the second moment is the mass-carrying moment M_2, this characteristic size is the mean mass-weighted size, D_{mmw}. The relationship between D_{eff} and D_{mmw} is characterized by Figs. 3a and 3b, respectively, which show the variation of ω_0 at a wavelength of 1.575 μm as a function of the characteristic sizes and T_c for all 20 662 F07 PSDs. In the case of D_{eff}, in the figures the same definitions are used as above. The figure shows that D_{eff} is simply some multiple of D_{mmw} and the spatial distribution of ω_0 in the spaces of characteristic size—T_c is exactly the same. Furthermore, the distribution of ω_0 shown in Figs. 3a and 3b is relatable to Fig. 1a. That is, at the same T_c values of $-80°$ and $-15°$C, small and large characteristic sizes can be chosen to give the same values of ω_0 for the same values of M_2 assumed above. The above figures illustrate that there is a choice to be made as to how the bulk ice optical properties are parameterized in climate models.

As is done in B014b and in this paper, we avoid relating the bulk ice optical properties to D_{eff} as is traditionally done. Instead, our choice is to relate the optical

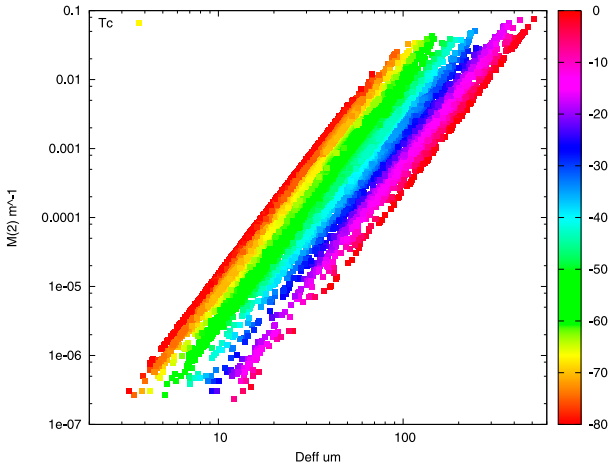

FIG. 2. The mass carrying moment M(2) as a function of the mean effective dimension, D_{eff}, and temperature, T_c, for all 20 662 values. The key on the right-hand side of the figure is T_c in units of °C.

properties directly to climate model prognostic variables such as M_2/IWC. This is because in climate models D_{eff} is generally diagnosed in the radiation scheme and the D_{eff} in the radiation scheme is different from the D_{eff} in the cloud physics scheme of a climate model because different PSDs are usually assumed. In the approach adopted by B014b and in this paper, we ensure that the PSDs generated through the F07 parameterization in the cloud physics scheme in the climate model are the *same* as those used in the radiation scheme, thus providing internal physical consistency within the climate model. In the traditional approach, this physical internal consistency is generally currently lost. Internal physical consistency could be satisfied using the traditional approach if D_{eff} were determined from the PSDs within the cloud physics scheme of the climate model and these values passed to the radiation scheme. In this way, the effective size then becomes consistent between the two schemes. However, this recovery of physical consistency requires an extra step within the climate model. Here, we prefer to avoid such an unnecessary step. It should also be noted that from Eq. (1), the integral over the mass requires some mass–D relationship to be applied. However, this mass–D relationship will obviously change depending on the choice of habit models; as a consequence, this has the potential to change the spatial distribution of ω_0 shown in Fig. 3a. However, in the approach adopted here, the mass of ice predicted by the climate model cannot change and, thus, will always be the same mass of ice between the cloud physics and radiation schemes.

In this paper, to generate the PSDs, the F07 moments are generated while assuming the recommended Furtado et al. (2015) mass–dimensional prefactor and exponent values of 0.0257 and 2.0, respectively, which were derived by Cotton et al. (2013), and by using the 20 662 IWC estimates and in-cloud temperature measurements compiled by B014a. Note that this mass–dimensional relationship is the same as that assumed by Hardiman et al. (2015), and was used by Vidot et al. (2015) to find the optimal ensemble model optical property parameterization that best simulated globally measured infrared radiometric brightness temperatures. Furthermore, in this paper, the weights assigned to each of the ensemble members at each F07 PSD bin size are the same as those assumed in experiment 4 of B014b [i.e., Eq. (9) in that paper], which were 0.50, 0.20, and 0.30, respectively. This assignment of weights to the ensemble model is different from that found by Vidot et al. (2015) to achieve radiometric equivalence between the model and measurements. However, experiment 4 of B014b gave the best comparisons between the climate model runs and space-based shortwave and longwave radiation measurements. In contrast, the Vidot et al. (2015) analysis is based on measurements obtained at three wavelengths in the infrared. It is yet to be seen whether the weightings found in that paper would remain the same if more solar and infrared wavelengths were to be utilized. This will be the subject of a future paper; thus, we assume the same weightings as those used in experiment 4 of B014b.

In the MetUM configuration of models, atmospheric particulates such as aerosol, ice, and water clouds are represented by vertical profiles of their mixing ratios with respect to air. In this paper and in B014b, the IWC becomes the ice mass mixing ratio, q_i, that is, the ratio between ice mass per unit volume and the mass of cloudy air per unit volume, and is in units of kg kg^{-1}. Likewise, the bulk optical properties, the volume extinction, and scattering coefficients become the mass extinction, K_{ext}, and mass scattering coefficients, K_{sca}, and both are in units of $\text{m}^2\,\text{kg}^{-1}$ (i.e., the extinction and scattering coefficients per unit mass of cloudy air).

In this paper, the bulk optical property database is first divided into the six shortwave and nine longwave Edwards–Slingo (Edwards and Slingo 1996, hereafter ES96) bands; these bands are defined in Table 1. In each of the ES96 bands, a total of about 10 000 q_i and T_c values were randomly selected from the bulk optical property database of B014a. Selected values of q_i and T_c were between 1.0×10^{-8} and $0.004\,\text{kg kg}^{-1}$ and −80° and 0°C, respectively. This randomly selected range in q_i–T_c space is sufficient to capture the full range that might be generated in an atmospheric model. In each of the ES96 bands, the bulk optical properties were parameterized as nonlinear and linear functions, dependent on q_i and T_c, by

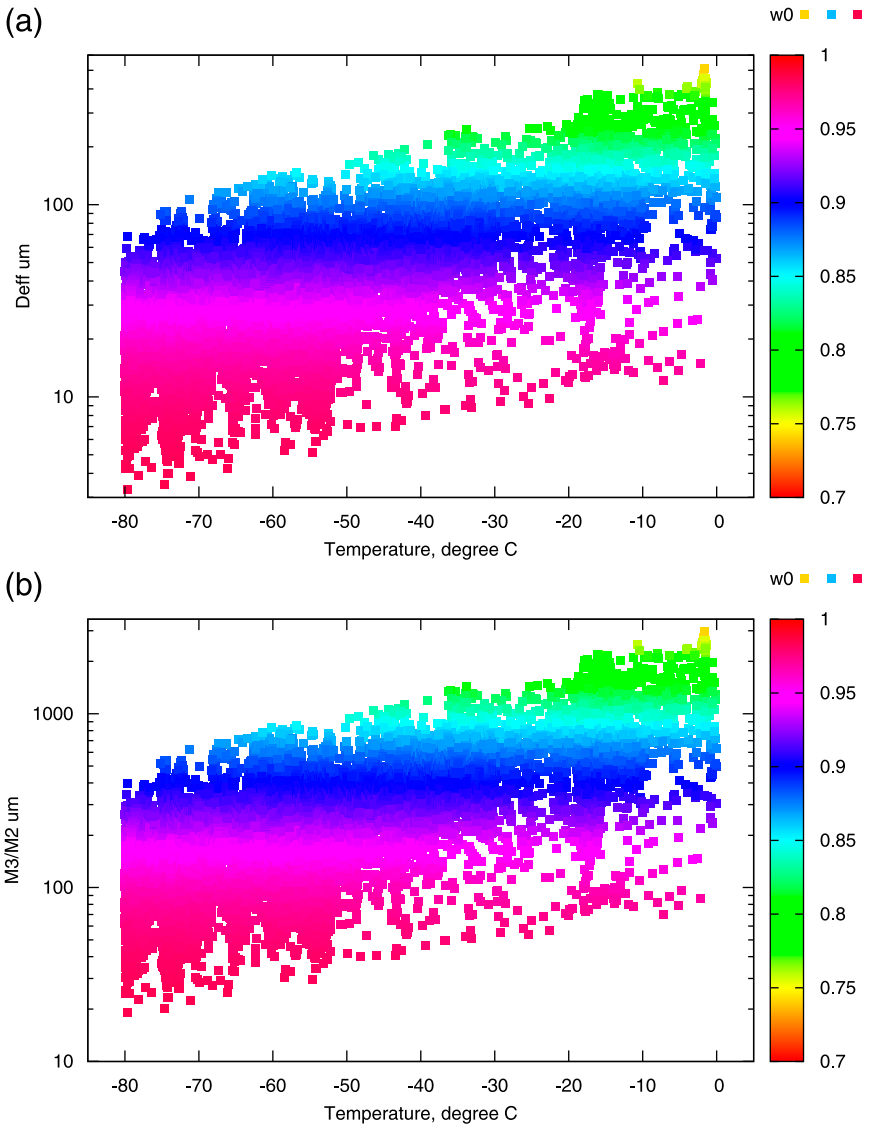

FIG. 3. The 20 662 calculated values of ω_0 as a function of (a) D_{eff} and (b) M3/M2, the mean mass-weighted size, D_{mmw}, of the PSD. The key on the right-hand side of the figures is the calculated values of ω_0 at the wavelength of 1.575 μm.

an iterative minimization procedure. That is, the forms of the parameterizations were first assumed and then the coefficients, for each of the parameterizations, were estimated by iterating through possible coefficient values. This was done until differences between the parameterizations and randomly selected 10 000 bulk optical properties were within acceptable experimental limits (i.e., estimated K_{ext} and K_{sca} values must be within $\pm 50\%$ of their true values for $>90\%$ of all possible q_i–T_c values). The error of $\pm 50\%$ in the mass coefficients is based on likely in situ errors in extinction estimates previously discussed in Baran et al. (2009). The errors resulting from this fitting procedure are discussed further below. The above fitting procedure resulted in the following best-fit bulk optical property parameterizations of cirrus:

$$K_{\text{ext}}(\lambda, q_i, T_c) = a_\lambda (q_i / T_c^4), \tag{2}$$

$$\omega_0(\lambda, q_i, T_c) = b_\lambda + c_\lambda q_i T_c, \tag{3}$$

$$g(\lambda, q_i, T_c) = d_\lambda + e_\lambda q_i T_c, \tag{4}$$

where the temperature, T_c, is in units of Kelvin. The ES96 estimated band-dependent coefficients a_λ, b_λ, c_λ, d_λ, and e_λ are listed in Table 1. It should be noted that to obtain the correct asymptotic behavior for $\omega_0(\lambda, q_i, T_c)$ and $g(\lambda, q_i, T_c)$, for the cases where $q_i > 10^{-3}\,\text{kg}\,\text{kg}^{-1}$,

TABLE 1. The derived values of the band-dependent coefficients for each of the ES96 shortwave and longwave bands. The first six entries in the table are the shortwave bands and the following nine entries are the longwave bands.

Band μm	a_λ	b_λ	c_λ	d_λ	e_λ
0.20–0.32	1.64×10^{11}	1.0000	6.5×10^{-15}	0.7560	0.0378
0.32–0.69	1.66×10^{11}	1.0000	-1.4×10^{-6}	0.7804	0.0419
0.32–0.69	1.64×10^{11}	0.9999	-6.4×10^{-5}	0.7860	0.0434
0.69–1.19	1.64×10^{11}	0.9996	−0.0031	0.7897	0.0468
1.19–2.38	1.65×10^{11}	0.9817	−0.4218	0.8208	0.1351
2.38–10.0	1.60×10^{11}	0.7500	−0.2353	0.9130	0.1240
25.0–10^4	1.50×10^{11}	0.6300	−0.2500	0.7129	0.6568
18.18–25.0	1.75×10^{11}	0.7700	−0.2866	0.8356	0.3085
12.50–18.18	1.73×10^{11}	0.5480	0.0108	0.8843	0.1833
13.33–16.95	1.74×10^{11}	0.5469	0.0146	0.8845	0.1730
8.33–12.50	1.44×10^{11}	0.5346	0.0106	0.9338	0.1013
8.93–10.10	1.54×10^{11}	0.6500	−0.1420	0.9401	0.1144
7.52–8.33	1.70×10^{11}	0.6000	−0.1781	0.9264	0.1513
6.67–7.52	1.72×10^{11}	0.6000	−0.1781	0.9331	0.1287
3.34–6.67	1.71×10^{11}	0.6009	−0.1304	0.9080	0.1762

the values of ω_0 and g should assume the same values as ω_0 and g when $q_i = 10^{-3}\,\mathrm{kg\,kg^{-1}}$. If this condition is applied, ω_0 and g should never attain unphysical values. In B014b the above bulk optical properties are expressed as functions of q_i only [i.e., Eqs. (4)–(7) in that paper]. This is possible to do, as shown by Fig. 2, and is equivalent to the parameterization proposed by McFarquhar et al. (2003). In that paper, as previously stated, the IWC is explicitly derived as a function of r_{eff}; in turn, the bulk optical properties are derived as a function of r_{eff}. Thus, r_{eff} can be eliminated between relationships to leave the bulk optical properties expressed as a function of IWC only, which is equivalent to B014b.

The difference between the above parameterization and that of B014b is highlighted by the following example. If we assume that $T_c = 190\,\mathrm{K}$ and $q_i = 1.0 \times 10^{-3}\,\mathrm{kg\,kg^{-1}}$, Eq. (3) at ES96 shortwave band 5 (1.19–2.38 μm) gives $\omega_0 = 0.9015$, while Eq. (6) from B014b gives $\omega_0 = 0.8663$. The former calculation is about 5% greater than the latter calculation, which means that in the former case the cirrus is about 27% less absorbing (i.e., $\sim 1 - \omega_0$) than in the latter case. With such a difference in shortwave absorption between the two parameterizations, the B014b parameterization is clearly more likely to result in an increase in TTL temperature than Eq. (3).

In the introduction to this paper, it was noted that trigonal ice crystals were observed by a number of studies in the TTL. Single-scattering calculations based on trigonal ice crystals using the anomalous diffraction approximation (ADT) have been reported by Murray et al. (2015). These calculations show that ω_0 values computed assuming trigonal columns can be as much as 20% higher than their equivalent hexagonal column counterparts for a range of crystal sizes they considered at an absorbing wavelength. If the TTL were composed mostly of trigonal columns, then this would imply less solar absorption and, as a consequence, less in-cloud heating, due to generally larger ω_0 values, relative to Eq. (3). However, ADT is a soft particle approximation (i.e., assumes real refractive indices near unity), originally due to van de Hulst (1957); by using this approximation, ω_0 values presented in Murray et al. (2015) may be overestimated (due to the neglect of reflection, refraction, and particle edge effects, which all tend to increase absorption; see, e.g., Mitchell et al. 2006). The latter limitations of ADT were noted by Murray et al. (2015), who also called for more accurate computations of the single-scattering properties of trigonal particles. On the other hand, if the TTL were composed of quasi-spherical particles as reported in some studies cited in the introduction to this paper, the calculated ω_0 values of these particles would tend to be lower (due to geometrical considerations and edge effects; see Baran and Havemann 1999; Mitchell et al. 2006; Bi and Yang 2014) than that calculated for the equivalent trigonal particles. This implies more absorption, and so greater in-cloud heating in the TTL, assuming equal microphysics assumptions. This range in potential TTL in-cloud heating is indicative of the current uncertainties in the microphysics composition within the TTL. Reducing uncertainty in calculated ω_0 values requires observations of PSDs, ice particle shapes, and application of electromagnetic methods and not gross approximations such as ADT to observed TTL microphysics measurements.

The accuracy of the new parameterizations was tested by selecting an independent set of about 10 000 q_i and T_c values taken from the ice optical property database of B014a. As before, the bulk optical properties, as a function of q_i and T_c, are grouped into their ES96 bands. The test of accuracy of the new parameterizations is based on the relative percent error, $\varepsilon(\lambda)$, which is given by

$$\varepsilon_\lambda = \frac{\mathrm{true}_\lambda - \mathrm{estimated}_\lambda}{\mathrm{true}_\lambda} \times 100\%, \qquad (5)$$

where in Eq. (5) true_λ and $\mathrm{estimated}_\lambda$ are the actual bulk optical properties in the B014b database consisting of 2.986×10^6 values (i.e., 20 662 q_i–T_c values × 145 wavelengths − 10 000 randomly selected values) and the estimated values using Eqs. (2)–(4), respectively. Here, the accuracy of the parameterizations is illustrated using only ES96 shortwave band 5 (1.19–2.38 μm), as all other bands have similar accuracies, and this band is important

for the shortwave heating of cirrus in the TTL. The calculated normalized PDFs of $\varepsilon(\lambda)$ are shown for $K_{\text{ext}}(\lambda, q_i, T_c)$, $K_{\text{sca}}(\lambda, q_i, T_c)$, and g in Figs. 4a–c, respectively. Figures 4a and 4b show that $\varepsilon(\lambda)$ in the mass parameterizations is within ±50% for about 90% and 94% of the independently selected database, respectively. Typically, the in situ measurement error in $K_{\text{ext}}(\lambda, q_i, T_c)$ is usually ±50% (Baran et al. 2009), so the relative error distribution shown in Figs. 4a and 4b is acceptable. Figure 4c shows $\varepsilon(\lambda)$ for g and, as can be seen from the figure, $\varepsilon(\lambda)$ is within ±2.5% for about 83% of the database, which is also acceptable. Theoretical and in situ uncertainty in the asymmetry parameter value is far greater than the error in the g parameterization (Ulanowski et al. 2006; Fu 2007; Garrett 2008; Baran 2012; van Diedenhoven et al. 2014). We compare our parameterization of g to the g parameterization developed by Fu (2007) by assuming q_i and T_c values of $1.0 \times 10^{-4}\,\text{kg kg}^{-1}$ and 190 K, respectively. In Fu (2007), g is parameterized in the shortwave by assuming hexagonal columns and hexagonal plates as a function of an effective AR by using either rough or smooth collections of particles. The range in the effective aspect ratio given by Fu (2007) represents the aspect ratios of monomer ice crystals that make up more complex ice crystals. Indeed, the effective AR of the ensemble model members assumed in this paper are 1.0, 0.42, and 0.42 (the first being the hexagonal ice column of AR = 1.0, and the latter two being the AR and averaged AR values found for the six-branched bullet rosette and the three monomer hexagonal ice aggregate, respectively), and the following weights of 0.50, 0.20, and 0.30 are assigned to the three ensemble members, respectively. The comparison is made by using the coefficients d_λ and e_λ tabulated in Table 1 at ES96 shortwave band 1 (i.e., 0.20–0.32 μm) and at ES96 shortwave band 3 (0.32–0.69 μm). These two shortwave bands cover the wavelength range given in Fu (2007) for shortwave band 1 (i.e., 0.25–0.70 μm) given in that paper. Although the comparison is not exact in terms of the wavelength range and assumed ice microphysics, it is considered sufficiently accurate for the purposes of this paper. Applying the above three effective AR ratios for each of the ensemble models to Eqs. (3.2) and (2.2) given in Fu (2007), and weighting the calculated asymmetry parameter values by the three weights given above, we find a weighted value of 0.765 for g (i.e., $0.5 \times 0.73 + 0.20 \times 0.80 + 0.3 \times 0.80$). This Fu (2007) asymmetry parameter value compares to the values of 0.757 and 0.787 found for ES96 shortwave bands 1 and 3, respectively, and the average of these two values is 0.772. The averaged value is within about 1% of the Fu (2007) calculation, and the values calculated at the two ES96 shortwave bands are within about ±2% of Fu (2007). If we take $g = 0.765$ and $g = 0.787$ (i.e., the most extreme difference) and assume that the cirrus is located over a dark ocean and conservative scattering, then the backward solar reflection is about 23.5% and 21.3%, respectively, where backward reflection $\sim(1 - g)$. The difference in reflected shortwave flux is at most about $7\,\text{W m}^{-2}$, assuming an area-averaged incident solar flux of $330\,\text{W m}^{-2}$, at least for the case considered here. These differences found for the g parameterizations are far less than the range in g found by several studies (Ulanowski et al. 2006; Fu 2007; Garrett 2008; Baran 2012; van Diedenhoven et al. 2014; Yang et al. 2015). Indeed, in the case of Ulanowski et al. (2006), experimentally derived g values were found to vary between 0.80 ± 0.04 and 0.63 ± 0.05 for smooth and rough ice analog rosettes, respectively, and this difference results in a shortwave flux uncertainty of about $-56\,\text{W m}^{-2}$. Furthermore, the calculated asymmetry parameter values using the two parameterizations compare well against radiometrically derived asymmetry parameter values using POLDER observations from van Diedenhoven et al. (2014). The observations from POLDER were located over the north coast of Australia. In that paper, at a T_c value of about −85°C, the asymmetry parameter values are shown to vary between about 0.74 ± 0.02 and 0.79 ± 0.04, which encompass the values of g, derived using the two completely different parameterizations. These experimental results obtained at 0.865 μm were roughly coincident with the three assumed shortwave bands used in the comparisons, and the imaginary index of ice is very weakly absorbing at all of the chosen shortwave bands as shown in B014b. At least at TTL temperatures, the parameterized g values derived in this paper appear representative of other independent derivations of g. However, g is one of the bulk ice optical properties that is important to constrain in climate models, as noted by Stephens et al. (1990). In this paper, we are concerned about TTL heating and specific humidity errors in a climate model, and these errors are more associated with the parameterizations found for $K_{\text{ext}}(\lambda, q_i, T_c)$ and $\omega_0(\lambda, q_i, T_c)$.

Equations (2) and (3) are now compared against the equivalent parameterizations developed by B014b. The parameterizations of g are not compared here as the results are not sufficiently different. In comparing the parameterizations a constant value of q_i is assumed, with its value being $1.0 \times 10^{-5}\,\text{kg kg}^{-1}$, while the temperature is allowed to vary between −80° and 0°C. The comparisons are shown in Figs. 5a–c at ES96 shortwave band 5 for $K_{\text{ext}}(\lambda, q_i, T_c)$, the coalbedo [i.e., $1 - \omega_0(\lambda, q_i, T_c)$], and $K_{\text{abs}}(\lambda, q_i, T_c)$ [i.e., $K_{\text{abs}}(\lambda, q_i, T_c) = K_{\text{ext}}(\lambda, q_i, T_c) - K_{\text{sca}}(\lambda, q_i, T_c)$], respectively. Other bands show generally

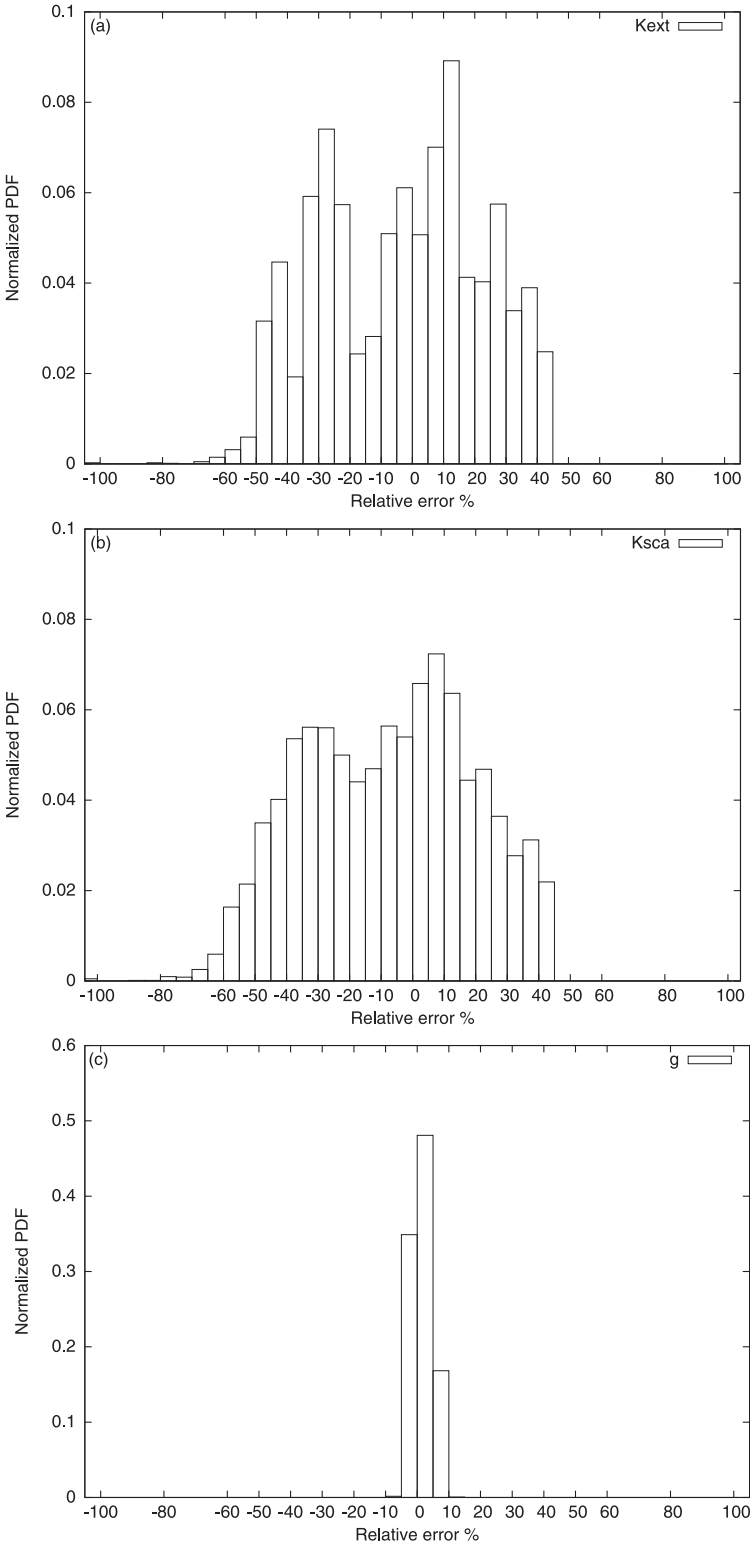

FIG. 4. The normalized PDFs of the relative percent error in the parameterization of (a) $K_{\text{ext}}(\lambda, q_i, T_c)$, (b) $K_{\text{sca}}(\lambda, q_i, T_c)$, and (c) $g(\lambda, q_i, T_c)$. Relative percent error results are shown for the ES96 shortwave band 5 (1.19–2.38 μm).

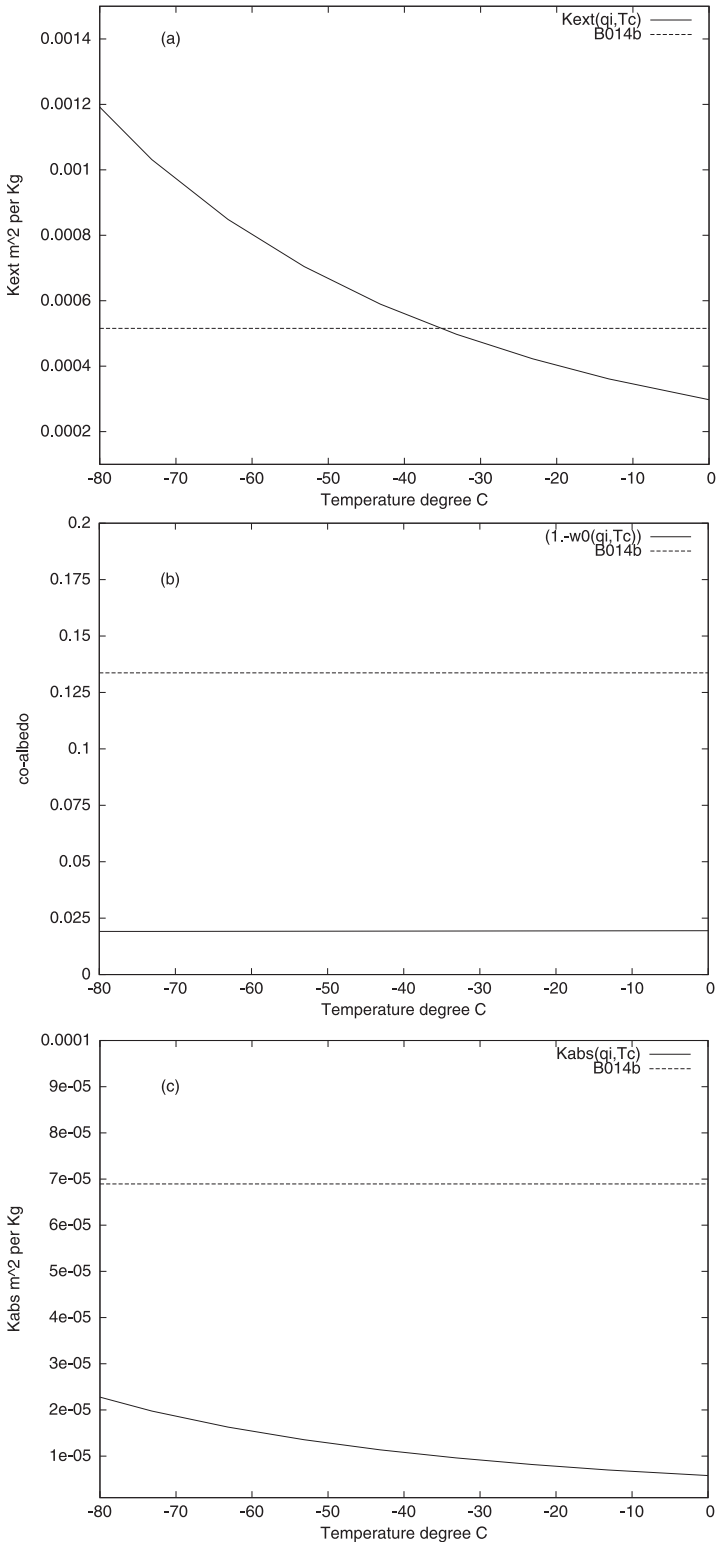

FIG. 5. Comparing the new parameterization (full line) to the B014b parameterization (dashed line) at the ES96 shortwave band 5 (1.19–2.38 μm). Comparisons are shown for (a) $K_{\text{ext}}(\lambda, q_i, T_c)$, (b) the coalbedo, and (c) $K_{\text{abs}}(\lambda, q_i, T_c)$.

similar results to Figs. 5a–c and are not shown here for reasons of brevity. Figure 5a shows that at T_c values of about −80°C, the nonlinear parameterization of $K_{\text{ext}}(\lambda, q_i, T_c)$ is about a factor of 2.5 greater than that predicted by B014b. This means that at typical TTL temperatures, the new parameterization, relative to B014b, will transmit less longwave terrestrial radiation to space through the cirrus, which will result in less longwave absorption by trace gases above the TTL cirrus, consequently lowering TTL temperatures through emission at cold temperatures. Also critical to the TTL temperature is the coalbedo. The coalbedo comparisons are shown in Fig. 5b; again, the figure shows that at $T_c = -80$°C, the new parameterization coalbedo is less than B014b by almost a factor of 7. This change in absorption between the parameterizations is shown clearly in Fig. 5c, which shows $K_{\text{abs}}(\lambda, q_i, T_c)$, and at $T_c = -80$°C, the new parameterization is almost 3 times less absorbing than B014b. The comparisons show that the temperature-dependent parameterization in the TTL should result in less cirrus heating relative to B014b. The next section presents the impact of these different heating profiles on the simulation of the TTL in an atmosphere-only climate integration using the MetUM.

3. The impact of the parameterizations on the simulation of the TTL

To assess the fidelity of the TTL simulation in models using the B014b parameterization and the parameterization described in section 2, we perform a pair of 20-yr atmosphere-only climate simulations using each parameterization. Apart from the formulation of the ice cloud optical properties, these simulations each use an identical baseline of the Global Atmosphere 6.0 (GA6.0) configuration of the MetUM. GA6.0 is the atmospheric component of the global coupled model 2.0 configuration as described by Williams et al. (2015), so a description is not repeated here. The simulations are performed at a horizontal resolution of N96 (~135 km in the midlatitudes) and use a vertical level set with spacings of between 500 and 700 m in the TTL region with a model "lid" at 85 km from the surface. The simulations run from December 1988 to November 2008 and use prescribed (but time varying) sea surface temperatures, greenhouse gas concentrations, and aerosol emissions while roughly following the protocol of the Atmospheric Model Intercomparison Project (AMIP; Taylor et al. 2012). Results are presented for the meteorological season December–February (DJF), as this season represents the period during which cirrus occurrence in the tropics is at a maximum (Sassen et al. 2008). The climate model predictions are compared against the ERA-Interim reanalysis temperature product (Dee et al. 2011) and the Modern-ERA Retrospective Analysis for Research and Applications (MERRA) specific humidity product (Rienecker et al. 2011). The impacts of the parameterizations on the 20-yr averaged DJF cloudy shortwave and longwave radiative effects at TOA are compared against the Loeb et al. (2009) reanalysis of the Clouds and the Earth's Radiant Energy System (CERES) product.

First, the DJF zonally averaged temperature differences between the B014b parameterization and the ERA-Interim reanalysis are shown in Fig. 6 (top left), while the same differences are shown in Fig. 6 (top right) but for the new parameterizations. It is clear from Fig. 6 (top right), relative to Fig. 6 (top left), that the new parameterizations have reduced the TTL temperature by about 1 K, and generally throughout the tropics, which is consistent with the discussion surrounding Figs. 5a and 5b. In addition, the new parameterization has also removed the warming in the southern subtropical troposphere region by about 1–2 K, and reduced cooling and warming over the South and North Poles, respectively. On the negative side, the new parameterizations lead to a cooling of the tropical troposphere by about 1 K, and to a similar cooling at altitudes between about 15 and 30 hPa, which occurs near the equator.

The impact of the new parameterizations on the model bias of zonally averaged $\log_{10}$ (specific humidity), relative to MERRA, is shown in Fig. 6 (bottom right). The figures show that the impact of the new parameterizations on the $\log_{10}$ (specific humidity) model bias in the TTL is to reduce it, and its distribution throughout the TTL, especially around the equatorial region. Relative to the B014b parameterization, shown in Fig. 6 (bottom left), the new parameterization reduces the $\log_{10}$ (specific humidity) model bias in the TTL by about 0.1 $\log_{10}$ (kg kg^{-1}) and generally reduces the extent of this bias in the subtropics. For each panel shown in Fig. 6, the grid point root-mean-square (RMS) errors were calculated over the region between 20°S and 20°N, and between 150 and 70 hPa. The resulting RMS errors were found to be 2.52, 1.90 K, and 0.13 and 0.12 $\log_{10}$ (kg kg^{-1}), respectively. Therefore, in the TTL region, the new parameterization reduces the zonally averaged temperature and specific humidity biases in the model.

Finally, to show that the new parameterizations do not result in any detriment to the climate model, in terms of the cloud radiative effect at TOA and global means, results are presented for the model's predicted radiative effects in Figs. 7a–d and global means in Table 2. The figures show that the new parameterization improves the shortwave and longwave cloud radiative effects in the climate model, relative to B014b. The extent of the shortwave bias in the model is significantly reduced, as

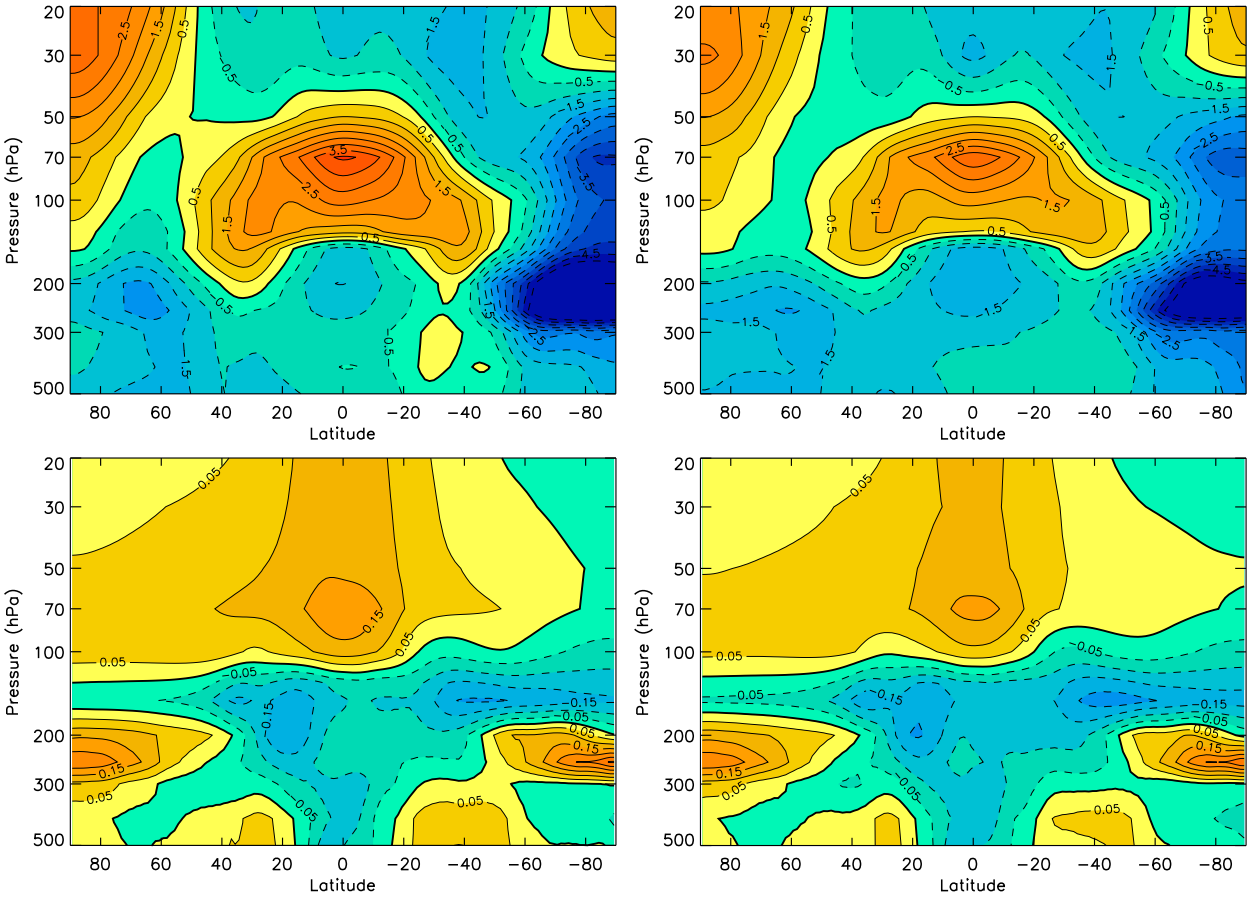

FIG. 6. The 20-yr DJF zonally averaged (top) temperature and (bottom) $\log_{10}$ (specific humidity) differences. The differences are between the MetUM configuration 6.0 run and the ERA-Interim and MERRA products, respectively. Results are shown while assuming (left) the B014b parameterization and (right) the new parameterization. The units of temperature difference and log (specific humidity) are K and $\log_{10}$ (kg kg^{-1}), respectively.

shown by the reduction in the area-weighted RMS error by 1.08 W m^{-2}, and this improvement is especially evident in the tropics. Note also the reduction in bias brought about by the new parameterization throughout the Southern Ocean. The longwave biases in the climate model are also reduced by the new parameterizations as shown in Figs. 7c and 7d, where it can be seen that the area-averaged RMS error is reduced by 0.41 W m^{-2}. The significant longwave negative biases around the warm pool shown in Fig. 7c have been reduced by the new parameterizations by up to about 20 W m^{-2}, as demonstrated by Fig. 7d.

Table 2 shows a comparison between the Stephens et al. (2012) estimated CERES global means for seven variables together with their estimated standard deviation $\pm\sigma$, and the B014b and temperature-dependent parameterizations. The table shows that the temperature-dependent parameterization is within the estimated uncertainty for six out of seven of the global mean variables shown in Table 2. This improves on the B014b parameterization, which has four out of seven variables within the estimated uncertainty. In particular, the B014b parameterization significantly underestimates the reflected shortwave flux at TOA. As a result of this underestimation, the predicted shortwave radiative effect is too low relative to the CERES estimated mean. The temperature-dependent parameterization does predict adequate reflected shortwave flux at TOA, but the prediction of the shortwave radiative effect is just over 1σ from the CERES estimated mean. This compares to about $1\frac{3}{4}\sigma$ from the estimated mean found for the B014b parameterization. The reason for this discrepancy between the parameterizations and the CERES observations for this variable is probably due to, in the case of B014b, the mass extinction coefficient being underestimated at about temperatures < -40°C, as can be seen from Fig. 5a, relative to the temperature-dependent parameterization. In the case of the temperature-dependent parameterization, the physical reasons for this underestimation could be that 1) there is too little ice mass being predicted by the model cloud

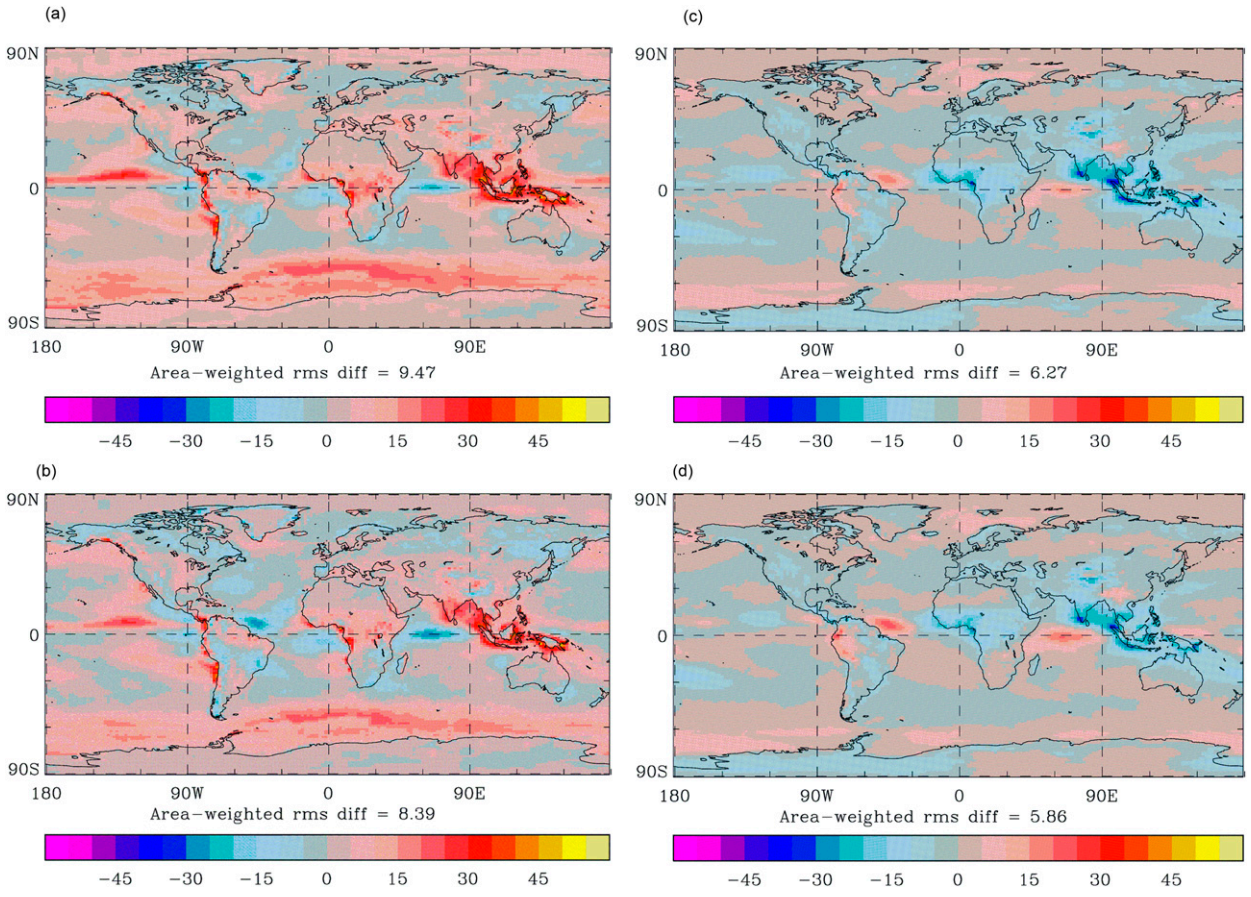

FIG. 7. The annual 20-yr TOA cloud radiative effect differences between MetUM configuration 6.0 and the CERES products. Results are shown for the shortwave while assuming the (a) B014b parameterization and (b) new parameterization. The longwave results are shown while assuming the (c) B014b parameterization and (d) new parameterization. The area-averaged root-mean-square difference is shown in each of the panels, and differences are in units of W m^{-2}.

scheme and/or 2) the model asymmetry parameter is too large. It is yet to be seen which of these reasons might account for the discrepancy in the shortwave radiative effect. However, in general, the new parameterization presented within this paper improves the model performance, relative to B014b, in terms of the shortwave and longwave cloudy radiative effect as can be seen from Figs. 7b–d, but also the predictions of model global mean fluxes.

4. Conclusions

A cirrus bulk optical property parameterization has been presented, and it has been demonstrated that the parameterization reduces zonally averaged temperature biases in the TTL of GA 6.0 by about 1–2 K relative to the B014b parameterizations. The parameterization of the asymmetry parameter was compared against an independent parameterization and was shown to be within about 1% and ±2% of the latter parameterization at ES96 shortwave bands 1 and 2, respectively. Moreover, the asymmetry parameters predicted by both parameterizations were shown to encompass space-based estimations of g from observations from around the north

TABLE 2. CERES means obtained from Stephens et al. (2012) compared against the MetUM configuration 6.0 means predicted using the B014b parameterization and the temperature-dependent parameterization. All flux units [shortwave (SW) and longwave (LW)] are in W m^{-2}. Asterisks denote that the predicted variable is within the current CERES measurement uncertainty, CF denotes cloud forcing.

Variable	Observation	B014b	Temperature-dependent
Outgoing SW	100 ± 2	97.58	99.66*
Outgoing LW	239.7 ± 3.3	240.53*	239.52*
Absorbed SW	240.2 ± 2	242.80	240.73*
Albedo TOA	29.41 ± 1	28.67*	29.28*
SW CF	−47.5 ± 3	−42.18	−44.23
LW CF	26.7 ± 4	23.88*	24.74*
Net surf SW	165 ± 6	168.64*	170.92*

coast of Australia at TTL cirrus temperatures of −85°C. The reason for this improvement in climate model performance is through coupling the bulk optical properties to q_i and T_c. At the low temperatures in the TTL, the B014b parameterization will underpredict the single-scattering albedo, resulting in TTL warming due, in part, to the absorption of shortwave radiation, highlighting the importance of wavelengths in the near-infrared. The new temperature-dependent parameterization also improves, relative to B014b, on representing the model's prediction of the shortwave and longwave cloudy radiative effect as well as global flux means. To improve climate model representations of the TTL, more careful consideration should be given to the calculation of ice optical properties, especially the mass extinction coefficients and single-scattering albedo, which are the bulk ice optical properties that principally determine the temperature and specific humidity distributions in our simulations of TTL cirrus. Further observations of cirrus PSDs, IWCs, habits (in addition to humidity and temperature measurements), and solar and infrared radiative properties in the TTL should be considered a priority.

Acknowledgments. The work of Steven C. Hardiman was supported by the joint DECC/Defra Met Office Hadley Centre Climate Programme (GA01101). Three reviewers are thanked for their contributions to this paper.

REFERENCES

Baran, A. J., 2009: A review of the light scattering properties of cirrus. *J. Quant. Spectrosc. Radiat. Transfer*, **110**, 1239–1260, doi:10.1016/j.jqsrt.2009.02.026.

——, 2012: From the single-scattering properties of ice crystals to climate prediction: A way forward. *Atmos. Res.*, **112**, 45–69, doi:10.1016/j.atmosres.2012.04.010.

——, and S. Havemann, 1999: Rapid computation of the optical properties of hexagonal columns using complex angular momentum theory. *J. Quant. Spectrosc. Radiat. Transfer*, **63**, 499–519, doi:10.1016/S0022-4073(99)00035-7.

——, and L.-C. Labonnote, 2007: A self-consistent scattering model for cirrus. 1: The solar region. *Quart. J. Roy. Meteor. Soc.*, **133**, 1899–1912, doi:10.1002/qj.164.

——, P. J. Connolly, and C. Lee, 2009: Testing an ensemble model of cirrus ice crystals using mid-latitude in situ estimates of ice water content, volume extinction coefficient, and the total solar optical depth. *J. Quant. Spectrosc. Radiat. Transfer*, **110**, 1579–1598, doi:10.1016/j.jqsrt.2009.02.021.

——, A. Bodas-Salcedo, R. J. Cotton, and C. Lee, 2011a: Simulating the equivalent radar reflectivity of cirrus at 94 GHz using an ensemble model of cirrus ice crystals: A test of the Met Office global numerical weather prediction model. *Quart. J. Roy. Meteor. Soc.*, **137**, 1547–1560, doi:10.1002/qj.870.

——, P. J. Connolly, A. J. Heymsfield, and A. Bansemer, 2011b: Using in situ estimates of ice water content, volume extinction coefficient, and the total solar optical depth obtained during the tropical ACTIVE campaign to test an ensemble model of cirrus ice crystals. *Quart. J. Roy. Meteor. Soc.*, **137**, 199–218, doi:10.1002/qj.731.

——, R. Cotton, K. Furtado, S. Havemann, L.-C. Labonnote, F. Marenco, A. J. Smith, and J.-C. Thelen, 2014a: A self-consistent scattering model for cirrus. Part II: The high and low frequencies. *Quart. J. Roy. Meteor. Soc.*, **140**, 1039–1057, doi:10.1002/qj.2193.

——, P. Hill, K. Furtado, P. Field, and J. Manners, 2014b: A coupled cloud physics–radiation parameterization of the bulk optical properties of cirrus and its impact on the Met Office Unified Model Global Atmosphere 5.0 configuration. *J. Climate*, **27**, 7725–7752, doi:10.1175/JCLI-D-13-00700.1.

Bi, L., and P. Yang, 2014: High-frequency extinction efficiencies of spheroids: Rigorous T-matrix solutions and semi-empirical approximations. *Opt. Express*, **22**, 10 270–10 293, doi:10.1364/OE.22.010270.

Corti, T., B. P. Luo, Q. Fu, H. Vömel, and T. Peter, 2006: The impact of cirrus clouds on tropical troposphere-to-stratosphere transport. *Atmos. Chem. Phys.*, **6**, 2539–2547, doi:10.5194/acp-6-2539-2006.

Cotton, R., S. Osborne, Z. Ulanowski, E. Hirst, P. H. Kaye, and R. S. Greenaway, 2010: The ability of the Small Ice Detector (SID-2) to characterize cloud particle and aerosol morphologies obtained during flights of the FAAM BAe-146 research aircraft. *J. Atmos. Oceanic Technol.*, **27**, 290–303, doi:10.1175/2009JTECHA1282.1.

——, and Coauthors, 2013: The effective density of small ice particles obtained from in situ aircraft observations of mid-latitude cirrus. *Quart. J. Roy. Meteor. Soc.*, **139**, 1923–1934, doi:10.1002/qj.2058.

Dee, D. P., and Coauthors, 2011: The ERA-Interim reanalysis: Configuration and performance of the data assimilation system. *Quart. J. Roy. Meteor. Soc.*, **137**, 553–597, doi:10.1002/qj.828.

Delanoë, J., and R. J. Hogan, 2010: Combined CloudSat-CALIPSO-MODIS retrievals of the properties of ice clouds. *J. Geophys. Res.*, **115**, D00H29, doi:10.1029/2009JD012346.

Deng, M., G. G. Mace, Z. Wang, and H. Okamoto, 2010: Tropical Composition, Cloud and Climate Coupling Experiment validation for cirrus cloud profiling retrieval using CloudSat radar and CALIPSO lidar. *J. Geophys. Res.*, **115**, D00J15, doi:10.1029/2009JD013104.

Edwards, J. M., and A. Slingo, 1996: Studies with a flexible new radiation code. I: Choosing a configuration for a large-scale model. *Quart. J. Roy. Meteor. Soc.*, **122**, 689–719, doi:10.1002/qj.49712253107.

——, S. Havemann, J.-C. Thelen, and A. J. Baran, 2007: A new parameterization for the radiative properties of ice crystals: Comparison with existing schemes and impact in a GCM. *Atmos. Res.*, **83**, 19–35, doi:10.1016/j.atmosres.2006.03.002.

Field, P. R., and A. J. Heymsfield, 2003: Aggregation and scaling of ice crystal size distributions. *J. Atmos. Sci.*, **60**, 544–560, doi:10.1175/1520-0469(2003)060<0544:AASOIC>2.0.CO;2.

——, ——, and A. Bansemer, 2006: Shattering and particle interarrival times measured by optical array probes in ice clouds. *J. Atmos. Oceanic Technol.*, **23**, 1357–1371, doi:10.1175/JTECH1922.1.

——, ——, and ——, 2007: Snow size distribution parameterization for midlatitude and tropical ice clouds. *J. Atmos. Sci.*, **64**, 4346–4365, doi:10.1175/2007JAS2344.1.

Foot, J. S., 1988: Some observations of the optical properties of clouds. II: Cirrus. *Quart. J. Roy. Meteor. Soc.*, **114**, 145–164, doi:10.1002/qj.49711447908.

Fu, Q., 2007: A new parameterization of an asymmetry factor of cirrus clouds for climate models. *J. Atmos. Sci.*, **64**, 4140–4150, doi:10.1175/2007JAS2289.1.

Furtado, K., P. R. Field, R. Cotton, and A. J. Baran, 2015: The sensitivity of simulated high clouds to ice crystal fall speed, shape and size distribution. *Quart. J. Roy. Meteor. Soc.*, **141**, 1546–1559, doi:10.1002/qj.2457.

Garrett, T., 2008: Observational quantification of the optical properties of cirrus cloud. *Light Scattering Reviews 3*, A. Kokhanovsky, Ed., Springer, 3–26.

Hardiman, S. C., and Coauthors, 2015: Processes controlling tropical tropopause temperature and stratospheric water vapor in climate models. *J. Climate*, **28**, 6516–6535, doi:10.1175/JCLI-D-15-0075.1.

Heymsfield, A. J., 1986: Ice particles observed in a cirriform cloud at −83°C and implications for polar stratospheric clouds. *J. Atmos. Sci.*, **43**, 851–855, doi:10.1175/1520-0469(1986)043<0851:IPOIAC>2.0.CO;2.

Holz, R. E., and Coauthors, 2016: Resolving ice cloud optical thickness biases between CALIOP and MODIS using infrared retrievals. *Atmos. Chem. Phys.*, **16**, 5075–5090, doi:10.5194/acp-16-5075-2016.

Hong, Y., and G. Liu, 2015: The characteristics of ice cloud properties derived from *CloudSat* and *CALIPSO* measurements. *J. Climate*, **28**, 3880–3901, doi:10.1175/JCLI-D-14-00666.1.

Houze, R. A., P. V. Hobbs, P. H. Herzegh, and D. B. Parsons, 1979: Size distributions of precipitation particles in frontal clouds. *J. Atmos. Sci.*, **36**, 156–162, doi:10.1175/1520-0469(1979)036<0156:SDOPPI>2.0.CO;2.

Jensen, E. J., and Coauthors, 2008: Formation of large (∼100 μm) ice crystals near the tropical tropopause. *Atmos. Chem. Phys.*, **8**, 1621–1633, doi:10.5194/acp-8-1621-2008.

——, and Coauthors, 2016: The NASA Airborne Tropical Tropopause Experiment (ATTREX): High-altitude aircraft measurements in the tropical western Pacific. *Bull. Amer. Meteor. Soc.*, doi:10.1175/BAMS-D-14-00263.1, in press.

Korolev, A. V., E. F. Emery, J. W. Strapp, S. G. Cober, and G. A. Isaac, 2013: Quantification of the effects of shattering on airborne ice particle measurements. *J. Atmos. Oceanic Technol.*, **30**, 2527–2553, doi:10.1175/JTECH-D-13-00115.1.

Lawson, R. P., B. Pilson, B. Baker, Q. Mo, E. Jensen, L. Pfister, and P. Bui, 2008: Aircraft measurements of microphysical properties of subvisible cirrus in the tropical tropopause layer. *Atmos. Chem. Phys.*, **8**, 1609–1620, doi:10.5194/acp-8-1609-2008.

Lee, J., P. Yang, A. E. Dessler, B.-C. Gao, and S. Platnick, 2009: Distribution and radiative forcing of tropical thin cirrus clouds. *J. Atmos. Sci.*, **66**, 3721–3731, doi:10.1175/2009JAS3183.1.

Letu, H., H. Ishimoto, J. Riedi, T. Y. Nakajima, C.-L. Labonnote, A. J. Baran, T. M. Nagao, and M. Skiguchi, 2015: Investigation of ice particle habits to be used for ice cloud remote sensing for the GCOM-C satellite mission. *Atmos. Chem. Phys. Discuss.*, **15**, 31 665–31 703, doi:10.5194/acpd-15-31665-2015.

Liou, K. N., 1986: Influence of cirrus clouds on weather and climate processes: A global perspective. *Mon. Wea. Rev.*, **114**, 1167–1199, doi:10.1175/1520-0493(1986)114<1167:IOCCOW>2.0.CO;2.

——, 2005: Cirrus clouds and climate. *McGraw-Hill 2005 Yearbook of Science & Technology*, McGraw-Hill, 51–53.

Loeb, N. G., B. A. Wielicki, D. R. Doelling, G. L. Smith, D. F. Keyes, S. Kato, N. Manalo-Smith, and T. Wong, 2009: Toward optimal closure of the Earth's top-of-atmosphere radiation budget. *J. Climate*, **22**, 748–766, doi:10.1175/2008JCLI2637.1.

Mace, G. G., Q. Zhang, M. Vaughan, R. Marchand, G. Stephens, C. Trepte, and D. Winker, 2009: A description of hydrometeor layer occurrence statistics derived from the first year of merged CloudSat and CALIPSO data. *J. Geophys. Res.*, **114**, D00A26, doi:10.1029/2007JD009755.

McFarquhar, G. M., A. J. Heymsfield, J. Spinhirne, and B. Hart, 2000: Thin and subvisual tropopause tropical cirrus: Observations and radiative impacts. *J. Atmos. Sci.*, **57**, 1841–1853, doi:10.1175/1520-0469(2000)057<1841:TASTTC>2.0.CO;2.

——, S. Iacobellis, and R. C. J. Somerville, 2003: SCM simulations of tropical ice clouds using observationally based parameterizations of microphysics. *J. Climate*, **16**, 1643–1664, doi:10.1175/1520-0442(2003)016<1643:SSOTIC>2.0.CO;2.

Mitchell, D. L., A. J. Baran, W. P. Arnott, and C. Schmitt, 2006: Testing and comparing the modified anomalous diffraction approximation. *J. Atmos. Sci.*, **63**, 2948–2962, doi:10.1175/JAS3775.1.

——, P. Rasch, D. Ivanova, G. M. McFarquar, and T. Nousiainen, 2008: Impact of small ice crystal assumptions on ice sedimentation rates in cirrus clouds and GCM simulations. *Geophys. Res. Lett.*, **35**, L09806, doi:10.1029/2008GL033552.

Murray, B. J., C. G. Salzmann, A. J. Heymsfield, S. Dobbie, R. R. Neely III, and C. J. Cox, 2015: Trigonal ice crystals in Earth's atmosphere. *Bull. Amer. Meteor. Soc.*, **96**, 1519–1531, doi:10.1175/BAMS-D-13-00128.1.

Rienecker, M. M., and Coauthors, 2011: MERRA: NASA's Modern-Era Retrospective Analysis for Research and Applications. *J. Climate*, **24**, 3624–3648, doi:10.1175/JCLI-D-11-00015.1.

Sassen, K., and B. S. Cho, 1992: Subvisual-thin cirrus lidar dataset for satellite verification and climatological research. *J. Appl. Meteor.*, **31**, 1275–1285, doi:10.1175/1520-0450(1992)031<1275:STCLDF>2.0.CO;2.

——, M. K. Griffin, and G. C. Dodd, 1989: Optical scattering and microphysical properties of subvisual cirrus clouds, and climatic implications. *J. Appl. Meteor.*, **28**, 91–98, doi:10.1175/1520-0450(1989)028<0091:OSAMPO>2.0.CO;2.

——, Z. Wang, and D. Liu, 2008: Global distribution of cirrus clouds from CloudSat/Cloud-Aerosol Lidar and Infrared Pathfinder Satellite Observations (CALIPSO) measurements. *J. Geophys. Res.*, **113**, D00A12, doi:10.1029/2008JD009972.

Schwartz, M. C., and G. G. Mace, 2010: Co-occurrence statistics of tropical tropopause layer cirrus with lower cloud layers as derived from CloudSat and CALIPSO data. *J. Geophys. Res.*, **115**, D20215, doi:10.1029/2009JD012778.

Sourdeval, O., C.-L. Labonnote, A. J. Baran, and G. Brogniez, 2015: A methodology for simultaneous retrieval of ice and liquid water cloud properties. Part I: Information content and case study. *Quart. J. Roy. Meteor. Soc.*, **141**, 870–882, doi:10.1002/qj.2405.

Stephens, G. L., S.-C. Tsay, P. W. Stackhouse Jr., and P. J. Flatau, 1990: The relevance of the microphysical and radiative properties of cirrus clouds to climatic feedback. *J. Atmos. Sci.*, **47**, 1742–1753, doi:10.1175/1520-0469(1990)047<1742:TROTMA>2.0.CO;2.

——, and Coauthors, 2012: An update on Earth's energy balance in light of the latest global observations. *Nat. Geosci.*, **5**, 691–696, doi:10.1038/ngeo1580.

Stubenrauch, C. J., F. Eddounia, J. M. Edwards, and A. Macke, 2007: Evaluation of cirrus parameterizations for radiative flux computations in climate models using TOVS–ScaRaB satellite observations. *J. Climate*, **20**, 4459–4475, doi:10.1175/JCLI4251.1.

Taylor, J., W. Randel, and E. J. Jensen, 2011: Cirrus cloud–temperature interactions in the tropical tropopause layer: A case study. *Atmos. Chem. Phys.*, **11**, 10 085–10 095, doi:10.5194/acp-11-10085-2011.

Taylor, K. E., R. J. Stouffer, and G. A. Meehl, 2012: An overview of CMIP5 and the experiment design. *Bull. Amer. Meteor. Soc.*, **93**, 485–498, doi:10.1175/BAMS-D-11-00094.1.

Ulanowski, Z., E. Hesse, P. H. Kaye, and A. J. Baran, 2006: Light scattering by complex ice-analogue crystals. *J. Quant. Spectrosc. Radiat. Transfer*, **100**, 382–392, doi:10.1016/j.jqsrt.2005.11.052.

van de Hulst, H. C., 1957: *Light Scattering by Small Particles*. Wiley, 544 pp.

van Diedenhoven, B., A. M. Fridlind, B. Cairns, and A. S. Ackerman, 2014: Variation of ice crystal size, shape, and asymmetry parameter in tops of tropical deep convective clouds. *J. Geophys. Res. Atmos.*, **119**, 11 809–11 825, doi:10.1002/2014JD022385.

Vidot, J., A. J. Baran, and P. Brunel, 2015: A new ice cloud parameterization for infrared radiative transfer simulation of cloudy radiances: Evaluation and optimization with IIR observations and ice cloud profile retrieval products. *J. Geophys. Res. Atmos.*, **120**, 6937–6951, doi:10.1002/2015JD023462.

Wang, L., and A. E. Dessler, 2006: Instantaneous cloud overlap statistics in the tropical area revealed by ICESat/GLAS data. *Geophys. Res. Lett.*, **33**, L15804, doi:10.1029/2005GL024350.

Westbrook, C. D., R. C. Ball, P. R. Field, and A. J. Heymsfield, 2004: Theory of growth by differential sedimentation, with application to snowflake formation. *Phys. Rev. E*, **70**, 021403, doi:10.1103/PhysRevE.70.021403.

Williams, K. D., and Coauthors, 2015: The Met Office global coupled model 2.0 (GC2) configuration. *Geosci. Model Dev.*, **8**, 1509–1524, doi:10.5194/gmd-8-1509-2015.

Yang, P., K.-N. Liou, L. Bi, C. Liu, B. Q. Yi, and B. A. Baum, 2015: On the radiative properties of ice clouds: Light scattering, remote sensing, and radiation parameterization. *Adv. Atmos. Sci.*, **32**, 32–63, doi:10.1007/s00376-014-0011-z.

Yang, Q., Q. Fu, and Y. Hu, 2010: Radiative impacts of clouds in the tropical tropopause layer. *J. Geophys. Res.*, **115**, D00H12, doi:10.1029/2009JD012393.

Yi, B., P. Yang, B. A. Baum, T. L'Ecuyer, L. Oreopoulos, E. J. Mlawer, A. J. Heymsfield, and K.-N. Liou, 2013: Influence of ice particle surface roughness on the global cloud radiative effect. *J. Atmos. Sci.*, **70**, 2794–2807, doi:10.1175/JAS-D-13-020.1.

Zhou, C., A. E. Dessler, M. D. Zelinka, P. Yang, and T. Wang, 2014: Cirrus feedback on interannual climate fluctuations. *Geophys. Res. Lett.*, **41**, 9166–9173, doi:10.1002/2014GL062095.